Reaction fronts, permeability and fluid pressure development during dehydration reactions

Henri LECLÈRE[a,*], Daniel FAULKNER[a], Sergio LLANA-FÚNEZ[b], John BEDFORD[a], John WHEELER[a]

[a] *Department of Earth and Ocean Sciences, University of Liverpool, 4 Brownlow Street, Liverpool, L69 3GP, UK*
[b] *Departamento de Geología, Universidad de Oviedo, calle Arias de Velasco s/n, 33005 Oviedo, Spain*

Keywords: `Reaction front, Gypsum dehydration, Permeability, Pore-fluid pressure, Compaction, Subduction zone`

Highlights :

1. Reaction fronts seen in nature are produced in laboratory during gypsum dehydration
2. Effective stress controls the development of wide or narrow reaction front
3. Reaction front velocity is faster for higher reaction rates, and slower the more compaction there is.

ABSTRACT

Fluids released by prograde metamorphism are often invoked to explain a range of crustal processes from earthquake triggering to metasomatism. These fluids can be either trapped and overpressured or released and channelized depending on the interplay between permeability, reaction rate and compaction. Experimental data are presented, measuring permeability, porosity and microstructural evolution throughout the dehydration of gypsum to form basanite. Reaction fronts, regions over which the reaction largely occurs, are used as a

*Corresponding author.
E-mail adress: **henri.leclere@liverpool.ac.uk** (Henri Leclère) *Tel:* **+44 (0)151 794 5149**

framework to explain the results. Experiments were conducted under hydrostatic conditions at a constant temperature of 115 °C at two effective pressures of 60 MPa and 110 MPa and three pore-fluid pressures of 20, 40 and 60 MPa. At high effective pressure, creep of the gypsum solid framework results in low porosity and permeability, producing high pore-fluid pressure build-up that slows the reaction rate. A clearly defined narrow reaction front migrates along the sample and the average permeability remains low until the front sweeps across the entire sample. Conversely, at low effective pressure the reaction front is wide producing a permeable, drained network. Average permeability is enhanced significantly after only a small fraction of the reaction has completed, by the interconnection of open pores. This study shows that the width of reaction fronts and hence the permeability development is strongly controlled by compaction. The reaction front velocity is broadly dependent on permeability and the reaction driving force. A simple quantitative model for these relationships is developed.

1. INTRODUCTION

Dehydration and devolatilization reactions are fundamental processes controlling fluid movement in the Earth. Dehydration reactions occur during prograde metamorphism when the increase of temperature causes hydrous minerals to become progressively unstable, break down and release water. Fluids released during reactions have been inferred to play an important role in key processes such as earthquake triggering and crustal melting in volcanic arc settings (Hacker et al., 2003; Miller et al., 2004; Abers et al., 2013; John et al., 2012). For instance, at intermediate depths in subduction zones (70-200 km), the development of locally high pore-fluid pressure during dehydration has been proposed as a mechanism to allow embrittlement at depths where the lithostatic pressure is typically considered to be too high to allow brittle deformation to occur (Raleigh and Paterson, 1965; Okazaki and Hirth, 2016). It has also been proposed that fluids from dehydration reactions can be channelized for long dis-

tances along the subduction interface, providing a route for water to be recycled back to the surface (Plümper et al., 2017; Angiboust et al., 2014; Scambelluri et al., 2015). The fate of fluids released by dehydration reactions, whether they become trapped and overpressured or drained and channelized, is strongly controlled by the permeability of the dehydrating rock which continuously evolves during reaction due to pore volume changes (Milsch et al., 2011; Tenthorey and Cox, 2003; Wang and Wong, 2003; Bedford et al., 2017). Changes of permeability and pore-fluid pressure have been shown previously to be key in controlling mechanical weakening during dehydration by changing the effective confining pressure (Milsch and Scholz, 2005; Proctor and Hirth, 2015; Brantut et al., 2012; Okazaki and Hirth, 2016; Leclère et al., 2016). Understanding how key physical properties such as permeability evolve during dehydration reactions is therefore fundamental for deciphering how high pore-fluid pressure can build up and also how trapped fluids in dehydrating rocks can be dissipated.

It has been shown that metamorphic devolatilization reactions can progress via a reaction front (Padrón-Navarta et al., 2011; Blattner, 2005). Reaction fronts may be defined as a region between mostly unreacted material and mostly reacted material. The permeability development in a dehydrating system must therefore be related in some way to the properties of these reaction fronts. Reaction fronts migrate from reacted material towards unreacted material (Fig. 1). They may be zones of measurable width, or narrow quasi 2D surfaces. In general, reaction fronts migrate according to how fluid overpressures generated by the reaction are able to dissipate. As dehydration reactions typically involve solid volume reductions, porosity is generated as reaction proceeds and thus the permeability of the reacting rocks is enhanced. Reaction fronts presumably migrate when fluids, moving perpendicular to the front, are able to drain from the unreacted material into the enhanced drainage architecture of the reacted rocks. Reaction front velocity is presumably dependent on how quickly fluids can escape and linked to permeability increase. In experiments described here, reaction fronts can be generated when excess pore-fluid pressure from a dehydrating sample is drained to an externally controlled reservoir at one end of the

sample (upstream reservoir) and is semi-undrained to an isolated reservoir on the other end (downstream reservoir) (Fig. 2).

Field studies of dehydrating systems, from exhumed fossil subduction zones, have shown two distinct dehydration structures: (1) narrow reaction fronts (Padrón-Navarta et al., 2011; Blattner, 2005), and (2) wide reaction fronts forming an anastomosing network of merging veins comprised of dehydration products having a distributed net-like structure (Taetz et al., 2016; Plümper et al., 2017). However, the current state of understanding does not include any detailed explanation of what influences reaction front width or velocity. A knowledge of the controlling factors would enable interpretation of preserved reaction fronts in terms of those factors, and prediction of velocities and hence large scale reaction and fluid flow rates. In this contribution compaction and reaction rate are shown to be key parameters controlling reaction front width and velocity. Reaction rate must be linked to front development, and compaction must have an effect in terms of reducing porosity and increasing fluid pressure. These effects were discussed by Wang and Wong (2003), although in their experiments reaction fronts were in most cases deduced indirectly from fluid expulsion behaviour. Many dehydration reactions are characterised by a solid volume decrease but a net volume increase if fluid pressure is kept fixed (e.g. serpentinite breakdown). Such reactions run faster when pore-fluid pressure is low; they can create their own porosity and permeability but evolving pore-fluid pressure will feedback on evolving reaction rate (Brantut et al., 2017; Connolly and Podladchikov, 1998). Compaction will also alter pore-fluid pressure and thus indirectly affect reaction rate. Here experiments are used to show how reaction and compaction interact to control reaction front behaviour, going beyond previous work by monitoring average permeability, separating and measuring effects of reaction and compaction, and characterising microstructures at multiple stages.

In this paper, the links between fluid pressure, permeability, deformation and reaction are explored during the development of wide/narrow and fast/slow reaction fronts. Reaction front width is shown to be controlled by the effective

confining pressure (defined as confining pressure minus the fluid pressure). At high effective confining pressures narrow fronts are promoted, as low permeability is maintained in the sample, allowing high pore-fluid pressure build-up which slows down the reaction rate. Reaction front velocity is broadly dependent on effective confining pressure and the reaction driving force with a slow reaction front for a high effective confining pressure and a slow reaction rate while for a low effective confining pressure and a fast reaction rate, a fast reaction front will develop. This study therefore provides a framework for characterizing the width and the velocity of reaction fronts and understanding how fluid pressure builds up and is dissipated during dehydration and devolatilization reactions.

2. EXPERIMENTAL METHODS

The reaction of gypsum ($CaSO_4$) to bassanite ($CaSO_4 0.5 H_2O$) is utilized in this study, as it acts as an analogue material for other hydrous minerals (*e.g.* serpentine, mica, lawsonite) with the advantage that its reaction can be closely controlled and that it allows a wide range of parameters to be explored. The reaction is associated with a solid volume reduction of 29% (mineral products only) and a net volume increase of 8% (mineral and fluid products) leading to fluid pressure build-up in an undrained system.

All tests are conducted under hydrostatic conditions at a constant temperature of 115°C and are designed to investigate how effective confining pressure (*i.e.* affecting compaction) and pore-fluid pressure (*i.e.* the driving force affecting reaction rate) combine to control permeability and fluid overpressure evolution during reaction front propagation. Two different constant effective confining pressures named hereafter HP_{eff} (effective confining pressure 110 MPa) and LP_{eff} (effective confining pressure 60 MPa) and three pore-fluid pressures named hereafter PP20, PP40 and PP60 for 20, 40 and 60 MPa respectively are analyzed. Fluid pressure is known to play a key role on the reaction rate while effective confining pressure effects pore compaction (Llana-Fúnez et al., 2012).

Cylindrical samples of intact Volterra gypsum with an initial mass (m_0) between 27.75 g and 28.80 g corresponding to a length of ∼40 mm and a diameter of ∼20 mm were prepared from the same block (Table 1). Samples were jacketed in a 3 mm thick Viton sleeve and two high permeability ($10^{-13}m^2$) stainless steel porous disks were placed at the top and bottom of the sample to evenly distribute the fluid pressure over the ends of the sample (Fig. 2). The samples were inserted into a hydrostatic pressure vessel with servo-controlled pore-fluid and confining pressure systems. Silicon oil is used as the confining medium. Two external furnaces between two external cooling jackets placed at the top and bottom of the pressure vessel provide a temperature control of 0.1°C, and a thermal gradient across the sample which is less than 1°C. Samples were saturated with distilled water after which confining pressure was increased to the target value and pore-fluid pressure was increased up to 90 MPa to inhibit the start of the dehydration reaction during temperature increase (Llana-Fúnez et al., 2012). When the temperature reached 115°C, pore-fluid pressure was decreased down to either 20, 40 or 60 MPa in order to start the reaction. For tests conducted at 80 MPa confining pressure and 20 MPa pore-fluid pressure, confining pressure was increased first to 110 MPa and then reduced to 80 MPa when the temperature reached 115°C and pore-fluid pressure was decreased down to 20 MPa.

The pore-fluid pressure is controlled only on one side of the sample whereas the other side is connected to an isolated small volume in order to monitor permeability. The pore pressure oscillation technique was used immediately once the starting experimental conditions were reached with two simultaneous fluid pressure oscillations of 90 and 900 seconds in order to cover a large range of permeability between 10^{-21} to $10^{-16}m^2$ (Fischer and Paterson, 1992; Bernabé et al., 2006). These values correspond to the lower and upper limits of permeability that can be measured with the experimental apparatus. A Fast Fourier Transform was used to identify the two frequencies and for computing the amplitude ratio and the phase shift required for the permeability calculation. The attenuation and phase lag are calculated from the upstream and downstream sig-

nals. From these two numbers the two dimensionless parameters of Fischer and Paterson were calculated (Fischer and Paterson, 1992). Their two simultaneous equations are reduced to one and then solved numerically (see AppendixA). The obtained permeability values are average values as dehydration reactions develop heterogeneously if a reaction front if present. The measured permeability during reaction front migration corresponds to harmonic average permeability with local permeability values being higher or lower in different parts of the sample (Song and Renner, 2006).

A displacement transducer on the pistons of the pore pressure pump and confining pressure pump provides a way to track the volume of fluid expelled from the sample as pressure is maintained (pore fluid volumometry) and also the volume of fluid introduced into the pressure vessel as the sample compacts (confining fluid volumometry). Pore fluid volumometry alone is unable to provide information on the reaction progress, as compaction will contribute to the volume of water expelled. However, as confining fluid volumometry records the net volume reduction of the sample from compaction, the total fluid volume expelled (recorded by pore fluid volumometry) minus the pore volume reduction (recoded by confining pressure volumometry) will give the amount of water expelled by the reaction alone and hence a proxy for the reaction extent in the sample. (The average reaction extent ξ and the evolution of average porosity ϕ displayed on Fig. 3 were thus computed using the initial mass m_0 of the sample and the pore-fluid and the confining-fluid volumometry (respectively Vol_{P_P} and Vol_{P_C}). The mass conservation equation formulated and clearly detailed by Brantut et al. (2012) in their Appendix A was adjusted to the experimental configuration used and used to compute ξ and ϕ (see Eqs 1 and 2) with T the temperature in the sample, T_0 the room temperature, ρ the density, M the molar mass, V the molar volume, *gyp* gypsum and *bas* bassanite (more details on Table 2).

$$\xi_{(t)} = \left[\rho_{water}(T_0)\left(\frac{Vol_{P_P(t)} - Vol_{P_C(t)}}{m_{(0)}/\rho_{gyp}}\right)\right] \Big/ \left[\left(\rho_{gyp}\frac{3M_{water}}{2M_{gyp}}\right) - \rho_{water}(T)\left(1 - \frac{V_{bas}}{V_{gyp}}\right)\right] \quad (1)$$

$$\phi_{(t)} = \xi_{(t)} \left(1 - \frac{V_{bas}}{V_{gyp}}\right) - \left(\frac{Vol_{P_C(t)}}{m_{(0)}/\rho_{gyp}}\right) \quad (2)$$

3. PERMEABILITY, POROSITY AND MICROSTRUCTURAL EVOLUTION RESULTS

The general behaviour for all experiments is the development of pore-fluid overpressures (maximum fluid pressure in the isolated downstream reservoir minus fluid pressure in the controlled upstream reservoir) at the onset of reaction followed by enhanced fluid drainage when the upstream and downstream reservoirs become fully connected until the end of the reaction (Fig. 3A). This breakthrough is related to the passage of a drainage front that is spatially and temporally related to the reaction front. This is defined as the zone where the pore-fluid pressure varies from excess, undrained values to drained values. In the experiments, the evolution of downstream pore-fluid pressure is used to define the onset of breakthrough as when pore-fluid pressure start to decrease (fluid loss is higher than fluid produces by the reaction). We assume that breakthrough is completed when fluid pressures in the upstream and downstream reservoirs are roughly equal. Both the effective confining pressure and pore-fluid pressure influence the overall reaction rate $\dot{\xi}$, the development of fluid overpressure, and the time for breakthrough (Fig. 3A-B). Higher effective confining pressure leads to an increase in the pore-fluid overpressure by a factor of ~ 3 between LP_{eff} and HP_{eff} conditions. Increasing pore-fluid pressure and/or effective confining pressure also slows the average reaction rate delaying the breakthrough from $\sim$ 4h for LP_{eff} and PP20 toward $\sim$ 20h for HP_{eff} and PP60. The time for fluid pressure equilibration or breakthrough can be converted to a velocity since it corresponds to the time for the leading edge of the drainage front to migrate through the length of the sample. The drainage front velocity follows the same trend as average reaction rate $\dot{\xi}$ and decreases when pore-fluid pressure or/and

confining pressure are increased. These results show that if reaction rate is high, reaction front velocity is fast. In the following, the evolution of porosity and permeability are analysed as a function of the reaction extent instead of time (Fig. 3C-D).

As reaction proceeds, the average porosity in all tests increases quasi-linearly due to a solid volume reduction as gypsum transforms to bassanite (Fig. 3C). Note that porosity values computed with Eq. 2 and shown in Fig. 3C correspond to average values for heterogeneous samples. It is clear that newly formed pores are not fully preserved as the maximum porosity values in Fig. 3C are lower than the theoretical 29% porosity predicted by stoichiometry. Pores are therefore simultaneously created and compacted during reaction, as is corroborated by the confining fluid volumometry. Compaction is greater at higher effective confining and pore-fluid pressures as shown by the slopes in Fig. 3C which decrease when effective confining and/or pore-fluid pressures are increased. Porosity decrease occurs by a combination of instantaneous mechanical compaction (e.g. (Bedford et al., 2018)) when increasing effective confining pressure and also time-dependent compaction as shown for the PP20 and PP40 tests where porosity decreases after the dehydration reaction reaches completion (green and red lines on Fig. 3C). The time-dependent compaction can also be seen by lower porosity values for a given reaction extent for experiments at the same effective confining pressure but higher pore-fluid pressure. Indeed, for a given effective confining pressure, increasing pore-fluid pressure slows down the reaction and therefore allows more time for compaction to occur. Porosity evolution during dehydration therefore results from the interplay of reaction that generates porosity and compaction that destroys it.

During the reaction, a rapid average permeability increase is recorded at the onset of breakthrough (see stars on Fig. 3D) up to a level broadly dictated by the effective confining pressure and pore-fluid pressure conditions with higher values for LP_{eff} than HP_{eff} and for PP20 than PP60 (Fig. 3D). These differences in average permeability are directly related to porosity reduction with respectively the lowest and highest porosity for $LP_{eff} - PP20$ and $HP_{eff} - PP60$

as shown in Fig. 3C. The average permeability increases and a change of trend occurs when average porosity exceeds values between 4 and 8% (see circles on Fig. 3C. Fluid pathways and permeability are efficiently developed for a small increase of porosity at the onset of reaction as shown by Tenthorey and Cox (2003) Wang and Wong (2003) and Bedford et al. (2017) (see stars on Fig. 3C). It can also be noted that the onset of the permeability increase occurs at lower average reaction extent for low pore-fluid pressure than high pore-fluid pressure (see stars on Fig. 3D). Conversely, effective confining pressure does not seem to have an effect on the average reaction extent at breakthrough (except for tests at PP40).

In order to understand how fluid pathways develop during the dehydration reaction, the evolving microstructure is analyzed from post-mortem samples collected at (i) the onset of reaction, (ii) during breakthrough and (iii) at the end of reaction (Figs. 4-5-7). Microstructures are remarkably different, with narrow reactions front for all HP_{eff} tests and wide reaction fronts for all LP_{eff} tests (Figs. 4-5-7). The thin section scans presented in Figures 4 and 7 clearly show the development of narrow reaction fronts for HP_{eff} tests with gypsum in white and bassanite highlighted by the blue dye in the associated porosity. Through time, narrow reaction fronts migrate from the drained side of the sample towards the undrained side (Fig. 4). Note that narrow reaction fronts travel faster along the edge of the sample and preserve gypsum in the middle (Fig. 4). Conceptually, it is expected that breakthrough for narrow reaction fronts should occur when reaction is close to completion. The data from the HP_{eff} tests show that breakthrough occurs when the average reaction extent is between $\sim$ 40 and 65% (Fig. 3A-B) This difference is likely due to a boundary effect at the contact between the sample and viton jacket. Narrow reaction fronts are well defined and occur over a length scale of $\sim$5mm (Fig. 5A). Within the region of these fronts, low-porosity gypsum aggregates are progressively incorporated as the front migrates, where they begin to dehydrate between aggregates of needle-shaped bassanite grains and associated porosity (Fig. 5C).

Conversely, LP_{eff} tests are not characterized by narrow reaction fronts; instead

the reaction front width is inferred to be greater than the length of the sample as shown in Figure 4 (see high resolution images in AppendixB, Figs. 4 and 5B to better identify bassanite needles). SEM images clearly show that wide reaction fronts arecharacterized by millimetre-sized bassanite needles appearing evenly distributed throughout the sample (Figs. 4 and 5B). Individual bassanite needles are surrounded by a moat-like pore space (Fig. 5D), which forms as a result of a solid volume reduction, as observed by Bedford et al. (2017) using synchrotron X-ray microtomography. Increased permeability arises when these moat-like pores become interconnected and form a drainage network between the unreacted gypsum.

4. DISCUSSION

4.1. Fluid pathways and fluid pressure development

In order to understand conceptually how reaction fronts and permeability develop during dehydration, Fig. 6 built on Fig. 1 illustrates the geometry of a reaction front but with the reference frame fixed to that of the front itself. Hence the velocity of the gypsum u_g entering the reaction front is not quite the same as the velocity of the bassanite u_b exiting the reaction front, after taking into account mass balance. There is an additional flux of water relative to this reference frame, as excess fluid volume is produced in the reaction and compaction of the porous framework also occurs. This reference frame will be used later to develop the analytical model. Fig. 6 also illustrates the relationship between a reaction front, defined in terms of reaction product proportion, and a drainage front, defined in terms of pressure drop.

Despite the apparently uniform distribution of bassanite in the LP_{eff} tests, the pressure data show breakthrough (Fig. 4). This leads to the inference that the drainage front is associated with only a small amount of reaction and its leading edge is contained within the reaction front. These are two distinct

features, although they move at the same speed. We propose that the drainage front is narrower than the reaction front (Fig. 6).

Consequently the trailing edge of the drainage front arrives at the downstream end significantly before the trailing edge of the reaction front. This explains how, particularly in the LP_{eff} tests, reaction remains incomplete after breakthrough. For example in Perm 28 (Fig. 4), the trailing edge of the drainage front has passed through the entire sample, but the trailing edge of the reaction front has not yet done so. Sharp reaction fronts (*e.g.* Perm 35) only form when their length scale is similar to the drainage front (*i.e.* narrow). This idea is developed into a quantitative model later in this section.

A synthesis of the data from this study is presented in Fig. 7. This figure shows the six experimental conditions, the maximum pore-fluid overpressures (maximum pore-fluid pressure minus starting pore-fluid pressure) and permeability that developed during dehydration reactions and the reaction front velocity calculated from the time at breakthrough (with data from Fig. 3A and synthesized in Table 2). Fig. 7 also shows the microstructures that developed at the breakthrough for four tests and the corresponding evolution of reaction, permeability and pore-fluid pressure inferred from the experimental data presented in Fig. 3.

Changes of porosity ϕ and associated permeability k during reaction will directly control fluid loss and pore-fluid pressure build-up. If the initial pore-fluid pressure is low enough, reaction will initiate homogeneously throughout the sample and induces a simultaneous increase of pore-fluid pressure and porosity. If the rate of reaction is rapid in comparison to the rate of fluid loss, pore-fluid pressure will increase until it suppresses the reaction. Conversely, if the rate of fluid loss is able to keep pace with the reaction rate, then reaction will progress uninhibited. The evolution of pore-fluid overpressures during dehydration reactions is thus directly related to two parameters. First the reaction rate $\dot{\xi}$, producing fluids, which is controlled by temperature and pore-fluid pressure. Secondly the compaction ε, expelling fluids, which depends on the porosity and the effective confining pressure (Ko et al., 1997; Wong et al., 1997; Wang and

Wong, 2003). Therefore, effective confining pressure controlling compaction and pore-fluid pressure controlling reaction rate can respectively be used as proxies for ε and $\dot{\xi}$.

Fig. 7 shows that the development of a narrow or a wide reaction front is highly dependent on the effective confining pressure and the development of pore-fluid overpressures in low permeability rock. The formation of either narrow reaction fronts for HP_{eff} tests or wide reaction fronts for LP_{eff} tests can be explained by a combined effect of pore-fluid overpressures which drastically slows down the reaction and effective confining pressure which prevents pore growth and permeability increase. Indeed, if the effective confining pressure is low, compaction will be low also, allowing porosity to increase and the development of high permeability fluid pathways forming an interconnected network between gypsum aggregates. A wide reaction front will therefore form with the dehydrated product distributed amongst the unreacted material. Conversely if low porosity is maintained by the high effective confining pressure, fluid overpressures will build-up and be unable to drain as a result of the very low initial permeability of gypsum below $10^{-19}m^2$. Any newly formed pores become 'frozen' due to the suppression of reaction and any compaction associated with reduced effective confining pressure conditions as the pore-fluid pressure increases. Reaction will therefore take place only at the drained interface and will progress via a narrow reaction front which liberates high pore-fluid pressure trapped in the low permeability unreacted material as it migrates. In nature a drained interface might be a fault zone, a fracture, or a lithological boundary. Gypsum alabaster has a very low starting porosity and permeability meaning that fluid can be efficiently overpressured at the onset of dehydration. If the fluid pressure during reaction exceeds the confining pressure sufficiently, hydrofracturing may occur and fractures could form preferential fluid pathways (Zhu et al., 2016). However, our microstructural observations did not show any hydrofractures forming suggesting that fluid overpressures did not exceed confining pressure and the tensile strength of gypsum. Fig. 7 also shows that if compaction ε is low in comparison to reaction rate $\dot{\xi}$, a fast-moving reaction front will form. Conversely, if

compaction ε is high in comparison to reaction rate $\dot{\xi}$ reaction front migration will be slow.

To test these general concepts, a simple analytical model has been developed (see AppendixC and Fig. 6). This analysis shows that the reaction front velocity (u_d) (Eq. 3) (assumed to be equal to the drainage front velocity), the drainage front width (w_d) and the reaction front width (w_r) *(Eqs.* 4 and 5) are determined by the reaction extent ξ_d, two dimensionless numbers η and ν, the water viscosity μ, a dimensionless number Z that depends on the density ratio between gypsum and bassanite, porosity ϕ_d at the trailing edge of the drainage front, $k(\phi_d)$ being the permeability there, $f(\Delta P)$ being the pressure related term in the reaction rate formula and ΔP being the difference between the pressure at the equilibrium P_{eq} and the pore-fluid pressure PP.

$$u_d = \left[\frac{\eta\nu}{\xi_d \mu Z}\right]^{1/2} \times [k(\phi_d) f(\Delta P) \Delta P]^{1/2} \tag{3}$$

$$w_d = \left[\frac{\xi_d \eta}{\nu \mu Z}\right]^{1/2} \times \left[\frac{k(\phi_d)\Delta P}{f(\Delta P)}\right]^{1/2} \tag{4}$$

$$w_r / w_d > \frac{\nu}{\xi_d} \ln\left(\frac{1-\xi_d}{1-\xi_f}\right) \tag{5}$$

Equations 3 and 4 are divided in two terms. At the left side are parameters that do not significantly vary between experiments, and another one at the right side is composed of the major parameters that have large differences between experiments; the latter explain the variations in reaction front width (w_d) *and reaction front velocity* (u_d). *Equation 3 shows that reaction front velocity is function of permeability* $k(\phi_d)$ *at the drained side of the sample and the reaction driving force. This means that if permeability is high and the driving force is high (i.e. low PP), reaction front velocity will be fast as shown in the experiments (see Fig. 7). On the contrary, if permeability is low and driving force low too (i.e. high PP), the reaction front velocity will be slow as shown in the experiments. A quantitative analysis has been conducted to compare experimental data with*

the results from the dimensional model (see Table 3). In Table 3 the theoretical reaction front velocity $\sqrt{k(\phi_d) \cdot f(\Delta P)\Delta P}$ is calculated, if we ignore the first term, with the reaction rate proxy $\dot{\xi}_{proxy}$ from Eq. 7 in Llana-Fúnez et al. (2012) and ΔP with the pressure at the equilibrium (Peq) equals to 115 MPa for 115°C(McConnell, 1987). We also tabulate the measured velocities from Table 1, averaged if there is more than one experiment for a particular set of conditions. For the two different effective pressures the measured and calculated velocities are normalized to the slowest velocity for that P_{eff}. The normalized experimental and modelled values are remarkably close and this indicates that the simple model is based on appropriate assumptions. Unfortunately, the same quantitative analysis cannot be conducted for the reaction front width since we could not determine the width of the reaction front during our experiments. However, a qualitative analysis of Equations 4 and 5 shows that the reaction front width is controlled, if the first term is ignored, by permeability and $f(\Delta P)/\Delta P$. Because of the division the reaction front width will not be sensitive to ΔP as $f(\Delta P) \cdot \Delta P$. Therefore, we would expect less effect of ΔP (*i.e.* pore-fluid pressure) on reaction front width than reaction front velocity. Reaction front width appears thus to be more controlled by permeability, which is function of compaction. This analysis is in agreement with the experimental data where reaction front width is strongly influenced by the effective confining pressure (Fig. 7). The three expressions (4), (3) and (5) thus provide a basis for explaining the general behaviour in the experiments, in terms of reaction front velocity and width.

4.2. Implications for dehydrating systems

This study shows that the interplay between metamorphism (*i.e.* reaction rate $\dot{\xi}$) and deformation (*i.e.* compaction rate $\dot{\varepsilon}$) is of primary importance in controlling the hydraulic properties of dehydrating rocks. The spatial distribution of reaction products in a dehydrating system (*i.e.* narrow or wide reaction fronts) has direct implications on deformation, fluid flow and reaction kinetics. For instance, Taetz et al. (2016) show preferential fluid flow in complex HP/LT

vein system (*i.e.* wide reaction front) cross-cutting eclogitic rocks of the Pouébo Eclogite Melange (northern New Caledonia) that formed from fluids released by metamorphic dehydration which then filled pore spaces, before being channelized into veins of variable size.

Natural examples of dehydrating systems have been preserved in fossil subduction zones. The Cerro del Almirez (CdA) massif located in southern Spain is one of the best exposures worldwide showing a narrow reaction front that formed during the breakdown of antigorite (antigorite -> talc + olivine + H2O) at $\sim$ 1.6 - 1.9 GPa and 680-710 °C(Padrón-Navarta et al., 2011). The narrow reaction front in CdA is comparable to those that form in the HP_{eff} tests presented in this work. Furthermore Padrón-Navarta et al. (2011) related the granoflesic texture in the dehydrated material to a high fluid pressure (*i.e.* low affinity reaction) which is in agreement with the high fluid overpressures that are associated with narrow reaction front development in the HP_{eff} tests here. Conversely, the Erro-Tobbio meta-serpentinites (ET-MS) located in the Ligurian Alps display distributed and interconnected anhydrous olivine veins that formed during the dehydration of antigorite (antigorite + brucite -> olivine + H2O) at 2.0 - 2.5 GPa and 550 - 650 °C(Plümper et al., 2017). These networks of dehydration veins, forming a wide reaction front described by these authors as finger-like structures are comparable to the LP_{eff} tests and are interpreted as preferential fluid pathways which channelize fluids that are a product from the dehydration reaction. Indeed, microstructures that developed in the LP_{eff} tests are characterized by interconnected pores around bassanite needles forming preferential fluid pathways in the unreacted material.

Based on this study, the development of a wide reaction fronts at ET-MS and a narrow reaction fronts at CdA would be expected to relate to differences in the effective confining pressure with a higher value at CdA than at ET-MS. However, the pressure at the peak of metamorphism for CdA is slightly lower than for ET-MS discarding a control by the confining pressure if the same pore-fluid pressure is assumed. One significant difference between the two settings is that the temperature at the peak of metamorphism is higher at CdA than ET-MS.

Viscous creep is activated by elevated temperature, meaning that the higher temperature at CdA could have a similar effect as the high effective confining pressure experiments in this study which promotes pore compaction, pore-fluid pressure increase and the development of a narrow reaction front. The effects of temperature on reaction front development have not been analysed in this study but, if it enhances the deformability of the system, it will also have an effect on the development of narrow reaction fronts. The antigorite dehydration reaction also differs between CdA and ET-MS with full antigorite out for CdA and antigorite+brucite dehydration for ET-MS. The abundance of brucite acting as chemical heterogeneities could lead to more localized dehydration and net-like structures as clearly shown by Plümper et al. (2017). The differences between CdA and ET-MS could thus be related to the abundance of brucite localizing the reaction. However, the experiments presented here show that narrow or wide reaction fronts can develop in homogeneous Volterra Gypsum and do not require a *sine qua non* heterogeneous reactant for the development of a net-like dehydration structure as shown by Plümper et al. (2017). This study provides a framework to understand the conditions that produce narrow reaction fronts versus wide reaction fronts and can therefore guide future research aiming to unravel the coupling between metamorphic reactions, deformation and fluid-flow.

5. CONCLUSIONS

Reaction progress, fluid pathway development and fluid pressure evolution have been investigated experimentally during gypsum dehydration at a temperature of 115°C, two effective confining pressures of 60 MPa and 110 MPa and three pore-fluid pressure of 20, 40 and 60 MPa. All experiments are characterized by a pore-fluid pressure increase at the onset of reaction followed by a reduction as the permeability in the sample increases related to the breakthrough of a migrating reaction front (and associated drainage front). The magnitude of the maximal pore-fluid pressure is lower at low effective confining pressures as breakthrough occurs more rapidly allowing excess fluid to dissipate.

Microstructural analysis shows that the difference between low and high effective confining pressure is associated with the development of wide and narrow reaction fronts respectively. Wide reaction fronts are characterized by evenly distributed bassanite grains which are surrounded by moat-like pores that connect early in the reaction to develop a network of preferential fluid pathways. Narrow reaction fronts are characterized by a sharp boundary ($\sim$ 5mm) between the low permeability unreacted gypsum and the well-drained product bassanite aggregates. The reaction front migrates towards the unreacted material as high pore-fluid pressures are able to dissipate. High effective confining pressure promotes compaction which maintains a low porosity and allows high pore-fluid overpressures to build-up. This also slows the overall reaction rate. Conversely, low effective confining pressure allows porosity to increase, enabling enhanced drainage and the dissipation of pore-fluid overpressures. Reaction front width is controlled by the effective confining pressure controlling permeability increase while reaction front velocity is controlled by the permeability and the reaction driving force. A slow reaction rate $\dot{\xi}$ and high compaction ε will maintain a low porosity, restricting fluid flow and hinder the progress of a migrating front. A narrow and slow reaction front will develop. Conversely a fast reaction rate $\dot{\xi}$ and a slow compaction ε will enhance porosity and permeability allowing the rapid migration of a reaction front in the early stages of a reaction. A fast and wide reaction front will develop. Finally, this study provides new understanding on the boundary conditions for the development of narrow and wide reaction fronts which are commonly observed in the field.

Acknowledgements

This work is supported by Natural Environment Research Council grant NE/J008303/1. Sarah Henton De Angelis and Michael Allen are deeply thanked for SEM analyses and G. Coughlan for assistance with the experimental equipment. Paul Hands is thanked for thin section preparation.

6. REFERENCES

Abers, G. A., Nakajima, J., van Keken, P. E., Kita, S., Hacker, B. R., 2013. Thermalpetrological controls on the location of earthquakes within subducting plates. Earth and Planetary Science Letters 369370, 178–187. URL http://www.sciencedirect.com/science/article/pii/S0012821X1300143X

Angiboust, S., Pettke, T., Hoog, D., M, J. C., Caron, B., Oncken, O., 2014. Channelized Fluid Flow and Eclogite-facies Metasomatism along the Subduction Shear Zone. Journal of Petrology 55 (5), 883–916. URL https://academic.oup.com/petrology/article/55/5/883/1494602/Channelized-Fluid-Flow-and-Eclogite-facies

Bedford, J., Fusseis, F., Leclère, H., Wheeler, J., Faulkner, D., 2017. A 4d view on the evolution of metamorphic dehydration reactions. Scientific Reports 7 (1), 6881. URL https://www.nature.com/articles/s41598-017-07160-5

Bedford, J. D., Faulkner, D. R., Leclère, H., Wheeler, J., 2018. High-Resolution Mapping of Yield Curve Shape and Evolution for Porous Rock: The Effect of Inelastic Compaction on Porous Bassanite. Journal of Geophysical Research: Solid Earth. URL http://onlinelibrary.wiley.com/doi/10.1002/2017JB015250/abstract

Bernabé, Y., Mok, U., Evans, B., 2006. A note on the oscillating flow method for measuring rock permeability. International Journal of Rock Mechanics and Mining Sciences 43 (2), 311–316. URL http://www.sciencedirect.com/science/article/pii/S1365160905000663

Blattner, P., 2005. Transport of low-aH2o dehydration products to melt sites via reaction-zone networks, Milford Sound, New Zealand. Journal of Metamorphic Geology 23 (7), 569–578.

URL http://onlinelibrary.wiley.com.liverpool.idm.oclc.org/doi/10.1111/j.1525-1314.2005.00595.x/abstract

Brantut, N., Schubnel, A., David, E. C., Héripré, E., Guéguen, Y., Dimanov, A., 2012. Dehydration-induced damage and deformation in gypsum and implications for subduction zone processes. Journal of Geophysical Research: Solid Earth 117 (B3), B03205.
URL http://onlinelibrary.wiley.com/doi/10.1029/2011JB008730/abstract

Brantut, N., Stefanou, I., Sulem, J., 2017. Dehydration-induced instabilities at intermediate depths in subduction zones. Journal of Geophysical Research: Solid Earth 122 (8), 2017JB014357.
URL http://onlinelibrary.wiley.com.liverpool.idm.oclc.org/doi/10.1002/2017JB014357/abstract

Connolly, J. A. D., Podladchikov, Y. Y., Mar. 1998. Compaction-driven fluid flow in viscoelastic rock. Geodinamica Acta 11 (2), 55–84.
URL http://www.sciencedirect.com/science/article/pii/S0985311198800065

Fischer, G. J., 1992. Chapter 8 The Determination of Permeability and Storage Capacity: Pore Pressure Oscillation Method. In: Wong, B. E. a. T.-f. (Ed.), International Geophysics. Vol. 51. Academic Press, pp. 187–211.
URL http://www.sciencedirect.com/science/article/pii/S0074614208628235

Fischer, G. J., Paterson, M. S., 1992. Chapter 9 Measurement of Permeability and Storage Capacity in Rocks During Deformation at High Temperature and Pressure. In: Wong, B. E. a. T.-f. (Ed.), International Geophysics. Vol. 51. Academic Press, pp. 213–252.
URL http://www.sciencedirect.com/science/article/pii/S0074614208628247

Hacker, B. R., Peacock, S. M., Abers, G. A., Holloway, S. D., 2003. Subduction factory 2. Are intermediate-depth earthquakes in subducting slabs linked to metamorphic dehydration reactions? Journal of Geophysical Research: Solid Earth 108 (B1), 2030.
URL http://onlinelibrary.wiley.com/doi/10.1029/2001JB001129/abstract

John, T., Gussone, N., Podladchikov, Y. Y., Bebout, G. E., Dohmen, R., Halama, R., Klemd, R., Magna, T., Seitz, H.-M., 2012. Volcanic arcs fed by rapid pulsed fluid flow through subducting slabs. Nature Geoscience 5 (7), 489–492.
URL http://www.nature.com.liverpool.idm.oclc.org/ngeo/journal/v5/n7/full/ngeo1482.html

Ko, S.-C., Olgaard, D. L., Wong, T.-F., 1997. Generation and maintenance of pore pressure excess in a dehydrating system 1. Experimental and microstructural observations. Journal of Geophysical Research: Solid Earth 102 (B1), 825–839.
URL http://onlinelibrary.wiley.com/doi/10.1029/96JB02485/abstract

Leclère, H., Faulkner, D., Wheeler, J., Mariani, E., 2016. Permeability control on transient slip weakening during gypsum dehydration: Implications for earthquakes in subduction zones. Earth and Planetary Science Letters 442, 1–12.
URL http://www.sciencedirect.com/science/article/pii/S0012821X16300267

Llana-Fúnez, S., Wheeler, J., Faulkner, D. R., 2012. Metamorphic reaction rate controlled by fluid pressure not confining pressure: implications of dehydration experiments with gypsum. Contributions to Mineralogy and Petrology 164 (1), 69–79.
URL http://link.springer.com/article/10.1007/s00410-012-0726-8

McConnell, J. D. C., 1987. The Pressure Dependence of the Dehydration of Gypsum to Bassanite. Mineralogical Magazine 51 (361), 453–457.
URL http://www.minersoc.org/pages/Archive-MM/Volume_51/51-361-453.pdf

Miller, S. A., Collettini, C., Chiaraluce, L., Cocco, M., Barchi, M., Kaus, B. J. P., 2004. Aftershocks driven by a high-pressure CO2 source at depth. Nature 427 (6976), 724–727.

Milsch, H., Priegnitz, M., Blöcher, G., 2011. Permeability of gypsum samples dehydrated in air. Geophysical Research Letters 38 (18), n/a–n/a.
URL http://onlinelibrary.wiley.com/doi/10.1029/2011GL048797/abstract

Milsch, H. H., Scholz, C. H., 2005. Dehydration-induced weakening and fault slip in gypsum: Implications for the faulting process at intermediate depth in subduction zones. Journal of Geophysical Research: Solid Earth 110 (B4), B04202.
URL http://onlinelibrary.wiley.com/doi/10.1029/2004JB003324/abstract

Okazaki, K., Hirth, G., 2016. Dehydration of lawsonite could directly trigger earthquakes in subducting oceanic crust. Nature 530 (7588), 81–84.
URL http://www.nature.com/nature/journal/v530/n7588/full/nature16501.html

Padrón-Navarta, J. A., Sánchez-Vizcaíno, V. L., Garrido, C. J., Gómez-Pugnaire, M. T., 2011. Metamorphic Record of High-pressure Dehydration of Antigorite Serpentinite to Chlorite Harzburgite in a Subduction Setting (Cerro del Almirez, Nevado-Filábride Complex, Southern Spain). Journal of Petrology 52 (10), 2047–2078.
URL http://petrology.oxfordjournals.org/content/52/10/2047

Plümper, O., John, T., Podladchikov, Y. Y., Vrijmoed, J. C., Scambelluri, M.,

2017. Fluid escape from subduction zones controlled by channel-forming reactive porosity. Nature Geoscience 10 (2), 150–156.
URL http://www.nature.com.liverpool.idm.oclc.org/ngeo/journal/v10/n2/full/ngeo2865.html

Proctor, B., Hirth, G., 2015. Role of pore fluid pressure on transient strength changes and fabric development during serpentine dehydration at mantle conditions: Implications for subduction-zone seismicity. Earth and Planetary Science Letters 421, 1–12.
URL http://www.sciencedirect.com/science/article/pii/S0012821X15001892

Raleigh, C. B., Paterson, M. S., 1965. Experimental deformation of serpentinite and its tectonic implications. Journal of Geophysical Research 70 (16), 3965–3985.
URL http://onlinelibrary.wiley.com/doi/10.1029/JZ070i016p03965/abstract

Scambelluri, M., Pettke, T., Cannaò, E., 2015. Fluid-related inclusions in Alpine high-pressure peridotite reveal trace element recycling during subduction-zone dehydration of serpentinized mantle (Cima di Gagnone, Swiss Alps). Earth and Planetary Science Letters 429, 45–59.
URL http://www.sciencedirect.com/science/article/pii/S0012821X15005038

Song, I., Renner, J., 2006. Experimental Investigation into the Scale Dependence of Fluid Transport in Heterogeneous Rocks. pure and applied geophysics 163 (10), 2103–2123.
URL http://link.springer.com.liverpool.idm.oclc.org/article/10.1007/s00024-006-0121-3

Taetz, S., John, T., Bröcker, M., Spandler, C., 2016. Fluid-rock interaction and evolution of a high-pressure/low-temperature vein system in eclogite from New Caledonia: insights into intraslab fluid flow processes. Contributions to

Mineralogy and Petrology 171 (11), 90.
URL http://link.springer.com.liverpool.idm.oclc.org/article/10.1007/s00410-016-1295-z

Tenthorey, E., Cox, S. F., 2003. Reaction-enhanced permeability during serpentinite dehydration. Geology 31 (10), 921–924.
URL http://geology.geoscienceworld.org.liverpool.idm.oclc.org/content/31/10/921

Wang, W.-H., Wong, T.-f., 2003. Effects of reaction kinetics and fluid drainage on the development of pore pressure excess in a dehydrating system. Tectonophysics 370 (1-4), 227–239.
URL http://www.sciencedirect.com/science/article/pii/S0040195103001884

Wong, T.-F., Ko, S.-C., Olgaard, D. L., 1997. Generation and maintenance of pore pressure excess in a dehydrating system 2. Theoretical analysis. Journal of Geophysical Research: Solid Earth 102 (B1), 841–852.
URL http://onlinelibrary.wiley.com/doi/10.1029/96JB02484/abstract

Zhu, W., Fusseis, F., Lisabeth, H., Xing, T., Xiao, X., De Andrade, V., Karato, S.-i., 2016. Experimental evidence of reaction-induced fracturing during olivine carbonation. Geophysical Research Letters 43 (18), 2016GL070834.
URL http://onlinelibrary.wiley.com.liverpool.idm.oclc.org/doi/10.1002/2016GL070834/abstract

Table 1: List of the experiments conducted in this study and sample properties. Reaction progress and volumetric mass are computed from the weight and volume of sample at the end of the experiments

Run number	PCeff (MPa)	PP (MPa)	m_0 (g)	Final Reaction progress (%)	Density ($kg.m^{-3}$)	Fluid Overpressure (MPa)	Time at breakthrough (h)	Speed ($mm.h^{-1}$)	Comments
Perm34	60	20	28.44	1.8	2313	/	/	/	Stop Before breakthrough
Perm29	60	20	28.15	8.2	2336	7.8	4.2	9.4	Stop at breakthrough
Perm20	60	20	28.49	101.5	2745	6.5	4.6	8.6	
Perm28	60	20	28.47	100.7	2749	7.3	3.5	11.4	
Perm21	60	40	28.45	99.9	2738	4.2	7.2	5.5	
Perm27	60	40	28.62	98.9	2768	5.5	7.0	5.7	
Perm22	60	60	28.36	99.8	2743	8.7	9.9	4.0	
Perm26	60	60	28.62	98.9	2734	8.3	11.8	3.4	
Perm40	60	60	28.50	17.0	2364	7.2	8.0	5.0	Stop at breakthrough
Perm10	110	20	27.75	95.0	2720	31.4	7.2	5.4	
Perm38	110	20	28.31	93.9	2765	33.6	7.6	5.3	
Perm44	110	20	28.80	46.6	2627	26.4	8.1	4.9	Stop at breakthrough
Perm23	110	40	28.53	100.0	2737	28.8	9.9	4.1	
Perm25	110	40	28.26	99.0	2749	32.2	10.1	3.9	
Perm32	110	60	28.61	12.0	2348	/	/	/	Stop Before breakthrough
Perm35	110	60	28.51	67.5	2563	26.5	19.6	2.0	Stop at breakthrough
Perm37	110	60	28.54	79.1	2631	24.8	21.2	1.9	
Perm19	110	60	28.25	95.2	2705	23.1	19.6	2.2	

Table 2: Parameter values used for computing reaction progress ξ and porosity θ evolution during gypsum dehydration

Parameter	Symbol	Value	Units
Density of gypsum	ρ_{gyp}	2305	$kg.m^{-3}$
Density of water at 20 MPa and 115 °C	ρ_{water}	956	$kg.m^{-3}$
Density of water at 60 MPa and 115 °C	ρ_{water}	974	$kg.m^{-3}$
Molar mass of water	M_{water}	18.0	$g.mol^{-1}$
Molar mass of gypsum	M_{gyp}	172.1	$g.mol^{-1}$
Molar volume of bassanite	V_{bas}	52.8 x 10^{-6}	$m^3.mol^{-1}$
Molar volume of gypsum	V_{gyp}	74.7 x 10^{-6}	$m^3.mol^{-1}$

Table 3: Reaction rate term, which forms part of Equation(AppendixC.14), normalised and compared to normalised observed velocities. P_{eq} corresponds to the equilibrium pressure at 115 °C which is equal to 115 MPa from McConnell (1987).

Quantity	Units						
Effective Confining Pressure (PC_{eff})	MPa	60	60	60	110	110	110
Pore-Fluid Pressure (PP)	MPa	20	40	60	20	40	60
Reaction rate proxy ($\dot{\xi}_{proxy}$) (from Llana-Fúnez et al. (2012)) with $\dot{\xi}_{proxy} = 10^{-16.9851+0.1142T-0.0127PP+0.0019Pc}$	s^{-1}	1.02E-04	5.67E-05	3.16E-05	1.27E-04	7.06E-05	3.93E-5
Reaction front velocity (v) $\approx \sqrt{\dot{\xi}_{proxy} \cdot (P_{eq} - PP)}$	$MPa^{\frac{1}{2}} s^{-\frac{1}{2}}$	98.4	65.2	41.70	109.70	72.8	46.5
Normalized Reaction front velocity computed (v)		2.36	1.56	1.00	2.36	1.56	1.00
Measured reaction front velocity (v) (see Fig. 7)	$mm.h^{-1}$	9.8	5.6	4.13	5.20	4.00	2.03
Normalized reaction front velocity measured (v)		2.37	1.36	1.00	2.56	1.97	1.00

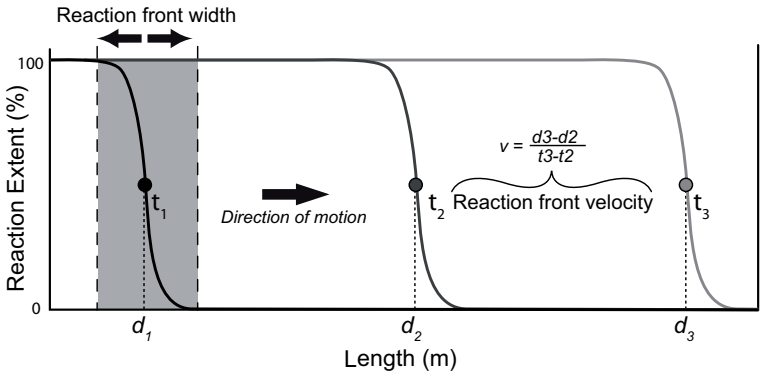

Figure 1: Schematic drawing explaining reaction front development.

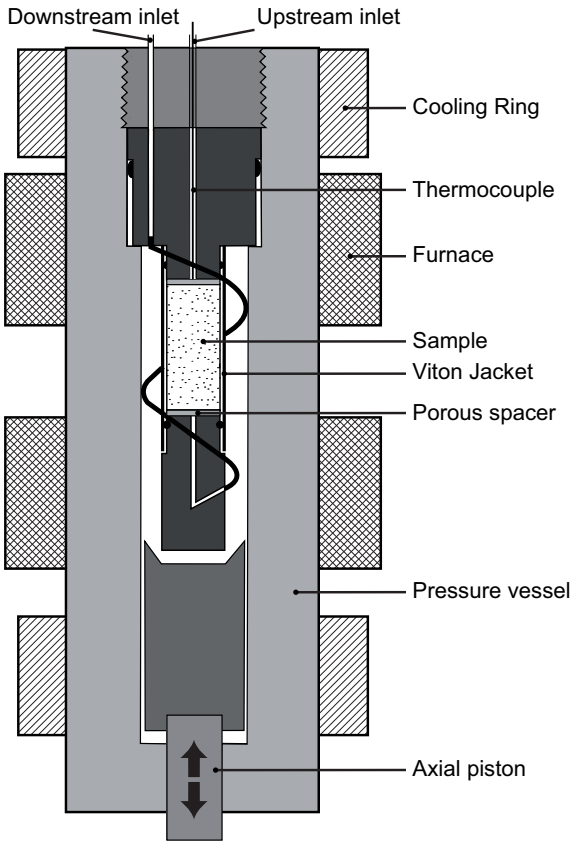

Figure 2: Schematic drawing of the pressure vessel and the sample assembly used in this study. All tests conducted in this study are hydrostatic (*i.e.* axial loading is not applied by the piston).

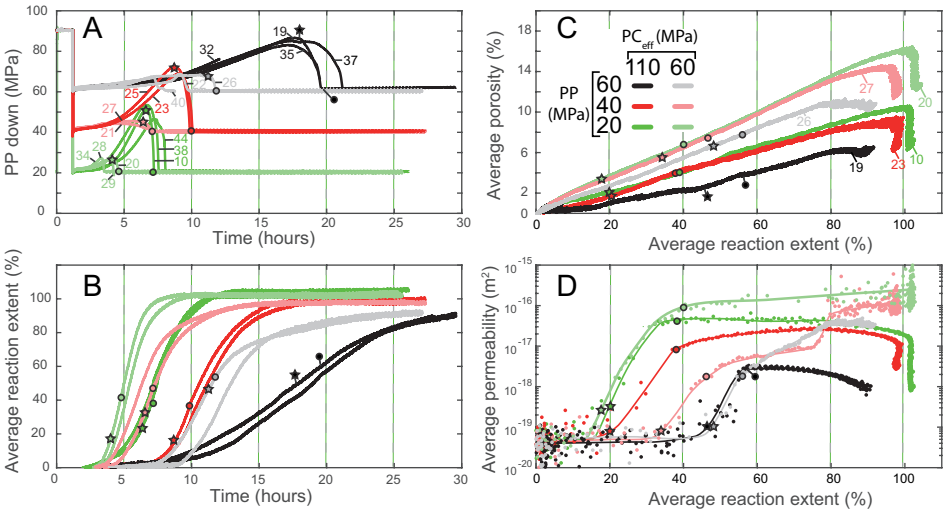

Figure 3: Results of dehydration reaction experiments conducted at two effective confining pressures of 60 and 110 MPa and three pore-fluid pressure of 20, 40 and 60 MPa. Stars indicate the onset of breakthrough while circles locate changes of the permeability trend and breakthrough when pore-fluid pressure equals in the upstream and downstream reservoirs. A: Evolution of pore-fluid pressure in the non-controlled downstream reservoir. Pore-fluid pressure gets higher for experiments conducted at effective confining pressure of 110 MPa than at 60 MPa. Breakthrough occurs later when pore-fluid pressure and/or effective confining pressure are increased. B: Reaction extent evolution through time for the different tested conditions. Reaction is faster and reaches completion earlier at low pore-fluid pressures and low effective confining pressures. C: Porosity evolution during reaction progress. Porosity increases linearly during the reaction and is lowered by increasing pore-fluid and effective confining pressures. Time-dependent compaction can be seen at the end of reaction where porosity decreases vertically. D: Permeability evolution during reaction progress characterized by a steep increase during breakthrough is followed by a plateau until the end of the reaction.

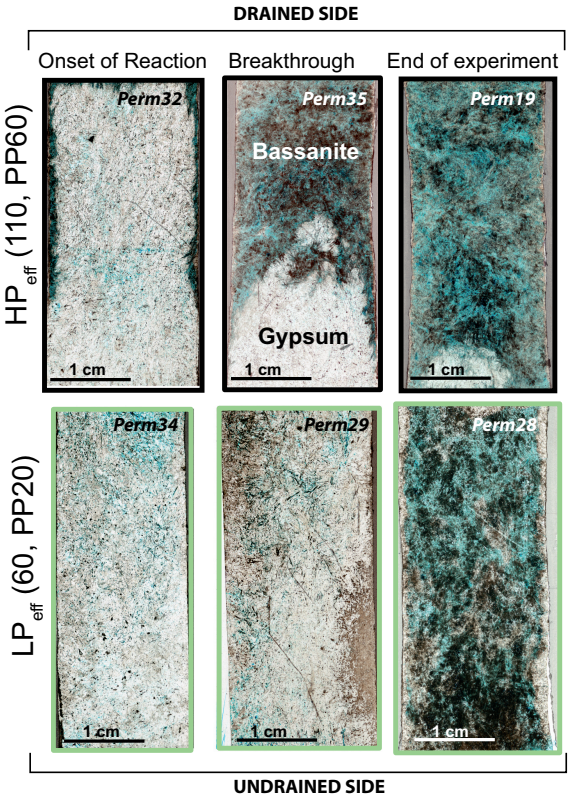

Figure 4: Thin section scans showing the evolution of microstructure during gypsum dehydration. HP_{eff} is characterized by a narrow reaction front while LP_{eff} is characterized by a wide reaction front. Blue color shows pores filled with blue-epoxy. Frame color refers to the color of the experiments in Fig. 3.

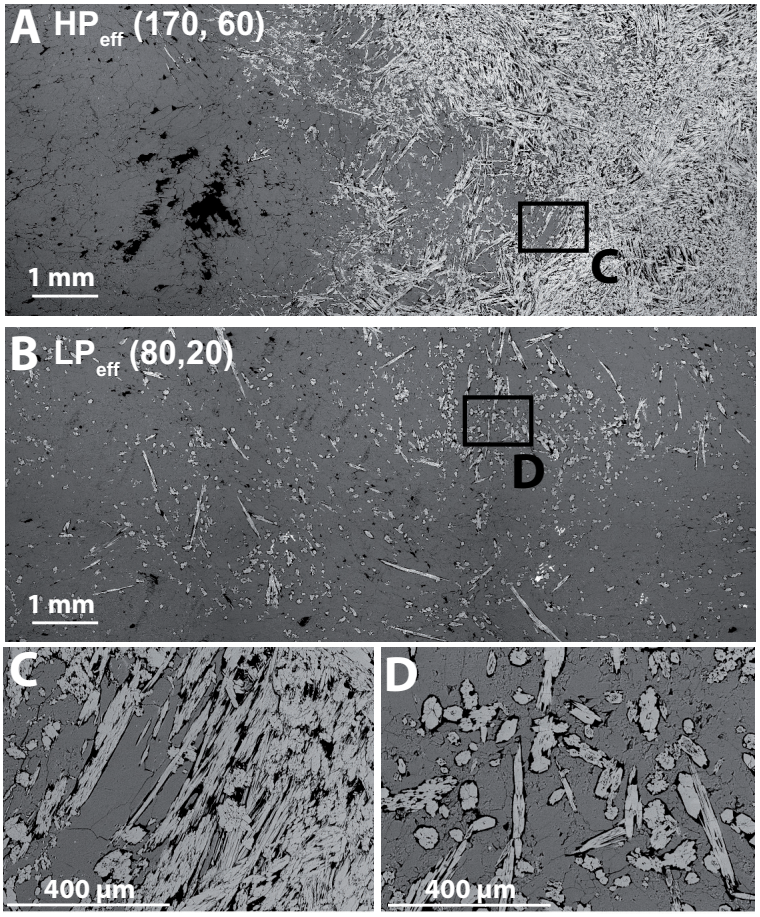

Figure 5: SEM micro-photographs showing the microstructures at the breakthrough for HP_{eff} and LP_{eff} tests. A: Narrow reaction front is characterized a sharp boundary separating bassanite in white and gypsum in grey. B: Wide reaction front is characterized by widespread millimeter-scale bassanite needles. C: Zoom on narrow reaction front showing gypsum aggregates pinched between bassanite needles. D: Zoom on wide reaction front showing bassanite needles surrounded by moats which connect to form preferential fluid pathways.

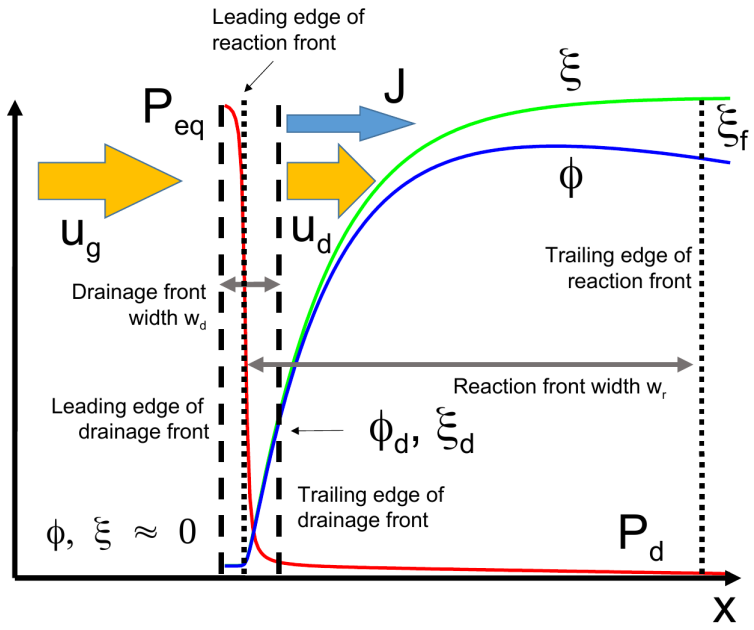

Figure 6: Conceptual model for reaction front and an associated drainage front, a region we define in this contribution as encompassing the main fluid pressure drop. The front is shown in a fixed position; gypsum moves from the left into the drainage front at speed ug and partially reacted material emerges at speed u_b, the difference in the two speeds indicating compaction. Pressure (red) drops from P_{eq}, assumed to be the value for chemical equilibrium, to P_d, the value at the drained end. Reaction progress x (green) climbs from near zero to near 1. Porosity (blue) climbs from zero to ϕ_d on exit from the drainage part of the front, at which point the flux of fluid evolved during dehydration is J; porosity continues to develop, but as reaction wanes compaction may become dominant and porosity decreases.

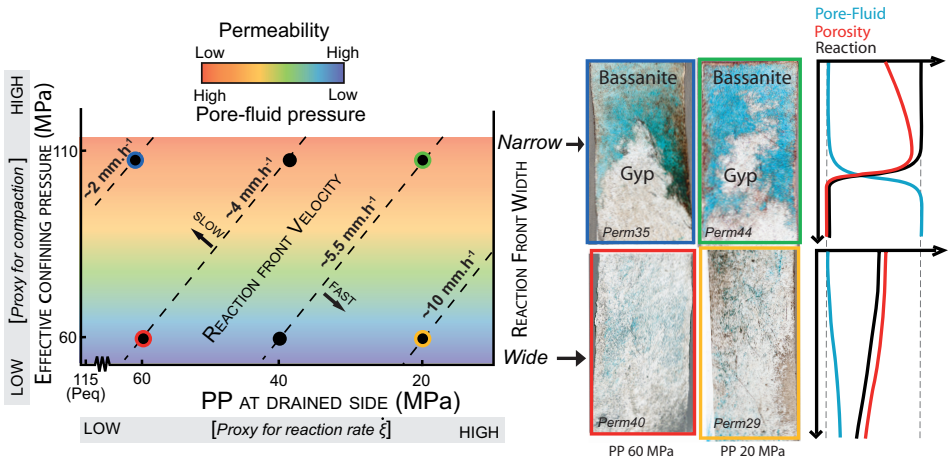

Figure 7: Graphic synthesising experimental data and microstructural observations. The development of a narrow reaction front is controlled by high effective confining pressure maintaining low permeability and allowing pore-fluid overpressure build-up. Reaction front velocity is broadly dependent on effective confining pressure and the reaction driving force with a slow reaction front for a high effective confining pressure and a slow reaction rate while for a low effective confining pressure and a fast reaction rate, a fast reaction front will develop.

AppendixA. Pore-Pressure Oscillation calculation

Following Fischer and Paterson (1992) we must solve two non-linear equation in two unknowns; equations in that work are referred to as (FP1) etc. for brevity. In what follows α is the attenuation and δ is the phase lag, which are measured. The two unknowns are expressed in dimensionless form as γ, the ratio (storage capacity of downstream reservoir)/(storage capacity of specimen), and ψ, related to permeability via (FP10). We calculate quantities X_D and Y_D, taking into account some notation confusion in (FP4). Fischer (1992) defines a variable θ as a function of position in his Eq. (9) but just above (FP4) this expression is reproduced as a formula for δ not θ. Fischer (1992) defines the upstream (imposed) pressure oscillation as

$$p_u = P_A \sin(\omega t + \delta) \qquad \text{(AppendixA.1)}$$

with the implication that the downstream pressure varies with $\sin(\omega t)$. Consequently the oscillatory part of Fischer (1992) (Eq.9) implies that at the downstream end we require $\delta = -\theta$. Thus (FP4) and the expression for Y_D in terms of δ require sign changes. Rewriting (FP7-8) we then have:

$$X_D = \cos(2\pi\delta)/\alpha \qquad \text{(AppendixA.2)}$$

$$Y_D = \sin(2\pi\delta)/\alpha \qquad \text{(AppendixA.3)}$$

and (FP8) is written as

$$X_D = \cosh\psi\cos\psi + \gamma\psi(\sinh\psi\cos\psi - \cosh\psi\sin\psi) \qquad \text{(AppendixA.4)}$$

$$Y_D = \sinh\psi\sin\psi + \gamma\psi(\sinh\psi\cos\psi + \cosh\psi\sin\psi) \qquad \text{(AppendixA.5)}$$

We have two equations in two unknowns. They are nonlinear and do not have closed form solutions. There are various ways in which to eliminate one unknown and solve for the other. We make a particular choice which we find does not lead to subsequent difficulties (e.g. divergence) in a numerical solution scheme. We eliminate γ and define a function $z(\psi)$ which must satisfy z = 0.

$$z = \cosh\psi\sinh\psi + \sin\psi\cos\psi + Y_D(\sinh\psi\cos\psi - \cosh\psi\sin\psi) - X_D(\sinh\psi\cos\psi + \cosh\psi\sin\psi); \qquad \text{(AppendixA.6)}$$

We solve this numerically for ψ using the Newton-Raphson technique and then calculate γ.

$$\gamma = \frac{X_D - \cosh\psi\cos\psi}{\psi(\sinh\psi\cos\psi - \cosh\psi\sin\psi)} \qquad \text{(AppendixA.7)}$$

The values of γ and ψ then give permeability and storativity using (FP9-10)

AppendixB. Supplementary Material

Supplementary material related to this article can be found online.

AppendixC. Reaction Front Model

We show that a simple mathematical model explains the general behaviour of our experiments. First we postulate that the reaction fronts (including their drainage fronts) are steady state and can viewed in a reference frame in which the front is fixed (Fig.6).

If the local matrix velocity is u (which varies with position because of compaction) then, by definition of steady state, for any property B, such as permeability or porosity, for example,

$$dB/dt = udB/dx \qquad \text{(AppendixC.1)}$$

We focus first on the drainage front, with width w_d. On leaving the drainage front, the fluid pressure has dropped to near P_d but the reaction has not finished, the progress being given by ξ_d (Fig.6) and the porosity by ϕ_d. In steady state, mass conservation dictates that the amounts of $CaSO_4$ and H_2O entering the front region must balance those components leaving it. We define ρ_g, ρ_b and ρ_w as the molar densities of gypsum, bassanite and water. At the trailing edge of the drainage front, the reaction is incomplete and solid density is given by $\rho_d = \rho_b\xi_d + \rho_g(1-\xi_d)$; here, sulphate mass conservation gives

$$\rho_g u_g = \rho_d(1-\phi_d)u_d \qquad \text{(AppendixC.2)}$$

Assuming zero initial porosity, and incompressible water for simplicity, H_2O mass conservation gives

$$2\rho_g u_g = \frac{1}{2}\rho_d(1-\phi_d)u_d + \rho_w\phi_d u_d + \rho_w J \qquad \text{(AppendixC.3)}$$

where the first term on the right relates to H_2O bound in the bassanite, the second relates to pore water moving with the moving porous medium and in the third term, J is the Darcy flux (volume/area/time) of water moving relative to the matrix because of pressure gradients.

Combining (AppendixC.2) and (AppendixC.3)

$$J = Zu_d \tag{AppendixC.4}$$

where

$$Z = \frac{3}{2}\frac{\rho_d}{\rho_w}(1-\phi_d) - \phi_d \tag{AppendixC.5}$$

The *local* reaction rate is $\dot{\xi}$, where $\xi = 1$ indicates complete reaction. It relates to other measures of reaction rate such as $\dot{\Gamma}$, defined as the volume of water released per unit bulk rock volume per unit time (following Wang and Wong (2003)), by $\dot{\xi} = \dot{\Gamma}/\Gamma_{max}$. It is dependent on the local difference between fluid pressure and that for equilibrium, and on X_g, the volumetric proportion of gypsum remaining. For illustration we select a simple dependency:

$$\dot{\xi} = X_g f(P_{eq} - P_f) \tag{AppendixC.6}$$

where $P_f(x)$ is local fluid pressure, P_{eq} is the pressure at chemical equilibrium and the function f describes the pressure dependence (in Wang and Wong (2003) it was power law). $\dot{\xi}$ varies across the front, but will be linked to the overall chemical drive. As the reaction progress is ξ_d after a material point has traversed the drainage front after time τ, the time integrated value is:

$$\int_0^\tau \dot{\xi} dt = \xi_d \tag{AppendixC.7}$$

and the average reaction rate is thus

$$\bar{\dot{\xi}} = \xi_d/\tau \cong \xi_d u_d/w_d \tag{AppendixC.8}$$

by virtue of the steady state assumption in Eq. (AppendixC.1) . The approximation is because matrix velocity is not equal to u_d everywhere, but is not significant as we are about to propose a dimensionless constant related to average reaction rate. Define

$$\Delta P = P_{eq} - P_d \tag{AppendixC.9}$$

where P_d is the pressure at the drained, downstream end. We postulate that across the reaction front the average reaction rate is

$$\bar{\dot{\xi}} = \nu f(\Delta P) \tag{AppendixC.10}$$

where ν is a dimensionless number less than 1 (because within the front, ΔP is less than that at the drained end, and X < 1). Combining Eq. (AppendixC.8) and Eq. (AppendixC.10)

$$u_d/w_d = \nu f(\Delta P)/\xi_d \tag{AppendixC.11}$$

Similarly we define a dimensionless number η representing the ratio of the local pore-fluid pressure gradient and pore-fluid pressure gradient over the drainage front such that at the "exit" from the drainage front

$$dP_f/dx = -\eta \Delta P/w_d \tag{AppendixC.12}$$

and this, together with Darcy's law at the trailing edge of the drainage front, gives

$$J = -\frac{k(\phi_d)}{\mu}\frac{dP_f}{dx} = \frac{k(\phi_d)\eta\Delta P}{\mu w_d} \tag{AppendixC.13}$$

Equations (AppendixC.4), (AppendixC.11) and (AppendixC.13) can be solved for the unknowns u_d and w_d.

$$u_d = \left[\frac{\eta\nu}{\xi_d \mu Z}\right]^{1/2} \cdot [k(\phi_d) f(\Delta P)\Delta P]^{1/2} \tag{AppendixC.14}$$

$$w_d = \left[\frac{\xi_d \eta}{\nu \mu Z}\right]^{1/2} \cdot \left[\frac{k(\phi_d)\Delta P}{f(\Delta P)}\right]^{1/2} \tag{AppendixC.15}$$

The expressions are split into two parts so as to make clear (as discussed in the main text) what the most important parameters are. We are now ready to look at the overall reaction front width w_r. Consider the evolution once the

drainage front has passed - in that region fluid pressure is close to P_d and, noting that $X_g = 1 - \xi$, the reaction rate eqn. (AppendixC.6) can be integrated

$$\xi = 1 - e^{-f(\Delta P)t} \tag{AppendixC.16}$$

We see that the reaction never truly finishes so define a notional "final" ξ_f close to but not equal to 1; then the time taken to evolve from ξ_d to ξ_f is

$$t = \frac{1}{f(\Delta P)} \ln\left(\frac{1-\xi_d}{1-\xi_f}\right) \cong w_q/u_d \tag{AppendixC.17}$$

We argue that ξ_f marks the trailing edge of the reaction front and hence define w_q as the width of that part of the reaction front beyond the drainage front. The total reaction front width is $w_r > w_q$ (there must be some overlap but we do not quantify this here). Combining eqns (AppendixC.11) and (AppendixC.17) we find

$$w_r/w_d > w_q/w_d = \frac{\nu}{\xi_d} \ln\left(\frac{1-\xi_d}{1-\xi_f}\right) \tag{AppendixC.18}$$

This shows that reaction front width scales with drainage front width.